

University of Groningen

Charge and spin transport in two-dimensional materials and their heterostructures

Bettadahalli Nandishaiah, Madhushankar

DOI:
[10.33612/diss.135800814](https://doi.org/10.33612/diss.135800814)

IMPORTANT NOTE: You are advised to consult the publisher's version (publisher's PDF) if you wish to cite from it. Please check the document version below.

Document Version
Publisher's PDF, also known as Version of record

Publication date:
2020

[Link to publication in University of Groningen/UMCG research database](#)

Citation for published version (APA):
Bettadahalli Nandishaiah, M. (2020). *Charge and spin transport in two-dimensional materials and their heterostructures*. [Thesis fully internal (DIV), University of Groningen]. University of Groningen.
<https://doi.org/10.33612/diss.135800814>

Copyright

Other than for strictly personal use, it is not permitted to download or to forward/distribute the text or part of it without the consent of the author(s) and/or copyright holder(s), unless the work is under an open content license (like Creative Commons).

The publication may also be distributed here under the terms of Article 25fa of the Dutch Copyright Act, indicated by the "Taverne" license. More information can be found on the University of Groningen website: <https://www.rug.nl/library/open-access/self-archiving-pure/taverne-amendment>.

Take-down policy

If you believe that this document breaches copyright please contact us providing details, and we will remove access to the work immediately and investigate your claim.

Downloaded from the University of Groningen/UMCG research database (Pure): <http://www.rug.nl/research/portal>. For technical reasons the number of authors shown on this cover page is limited to 10 maximum.

7 Large spin-relaxation anisotropy in bilayer-graphene/ WS₂ heterostructures

Abstract

We study spin-transport in bilayer-graphene (BLG), spin-orbit coupled to a tungsten disulfide (WS₂) substrate, and measure a record spin lifetime anisotropy $\sim 40-70$, i.e. the ratio between the out-of-plane τ_{\perp} and in-plane spin relaxation time τ_{\parallel} . We control the injection and detection of in-plane and out-of-plane spins via the shape-anisotropy of the ferromagnetic electrodes. We estimate $\tau_{\perp} \approx 1-2$ ns via Hanle measurements at high perpendicular magnetic fields and via a new tool we develop: oblique Spin Valve measurements. Using Hanle spin-precession experiments we find a low $\tau_{\parallel} \approx 30$ ps in the electron-doped regime which only weakly depends on the carrier density in the BLG and conductivity of the underlying WS₂, indicating proximity-induced spin-orbit coupling (SOC) in the BLG. Such high τ_{\perp} and spin lifetime anisotropy are clear signatures of strong spin-valley coupling for out-of-plane spins in BLG/WS₂ systems in the presence of SOC and unlock the potential of BLG/transition metal dichalcogenide heterostructures for developing future spintronic applications.

Published as:

S. Omar, **B.N. Madhushankar**, and B.J. van Wees,

Physical Review B 100 (15), 155415 (2019).

7.1 Introduction

Graphene (Gr) in contact with a transition metal dichalcogenide (TMD), having high intrinsic spin-orbit coupling (SOC), offers a unique platform where the charge transport properties in Gr are well preserved due to the weak van der Waals interaction between the two materials. However, the spin transport properties are greatly affected due to the TMD-proximity induced SOC in graphene¹⁻³. At the Gr/TMD interface, the spatial inversion symmetry is broken, and the graphene sublattices having $K(K')$ valleys experience different crystal potentials and spin-orbit coupling magnitudes from the underlying TMD. The electron-spin degree of freedom and its interaction with other properties such as valley pseudospins in the presence of SOC provide access to spintronic phenomena such as spin-valley coupling⁴⁻⁹, spin-Hall effect^{10,11}, (inverse) Rashba-Edelstein effect¹²⁻¹⁶, and even topologically protected spin-states¹⁷⁻²¹ which are not possible to realise in pristine graphene. The mentioned effects are sought after for realising enhancement and electric field control of SOC^{1,3,22-26}, efficient charge-current to spin-current conversion and vice versa^{10,27-29}, which will be the building blocks for developing novel spintronic applications^{13,30}.

Experiments on Gr/TMD systems confirm the presence of enhanced spin-orbit coupling^{3,31} and the anisotropy in the in-plane (τ_{\parallel}) and out-of-plane (τ_{\perp}) spin relaxation times^{7,9,32} in single layer graphene. Recent theoretical studies^{22,23} predict that due to the special band structure of bilayer graphene on a TMD substrate, it is expected to show a larger spin-relaxation anisotropy $\eta = \frac{\tau_{\parallel}}{\tau_{\perp}}$ even up to 10000²³, which is approximately 1000 times higher than the highest reported η values for single-layer graphene-TMD heterostructures^{9,33}. As explained in Ref.[23], a finite band-gap opens up in bilayer graphene (BLG) in the presence of a built-in electric field at the BLG/TMD interface, which can be tuned via an external electric field. The BLG valence (conduction) band is formed via the carbon atom orbitals at the bottom (top) layer. As a consequence, due to the closer proximity of the bottom BLG layer with the TMD, the BLG valence band has almost two order higher magnitude of SOC of spin-valley coupling character than the SOC in the conduction band. This modulation in the SOC can be accessed in two ways: either by the application of a back-gate voltage by tuning the Fermi energy or via the electric-field by changing the sign of the orbital gap. Depending on whether the graphene is hole or electron doped, and the magnitude of the electric field at the interface, BLG can therefore exhibit the effect of spin-valley coupling in the magnitude of spin-relaxation anisotropy ratio η .

In this paper, we report the transport of both in-plane and out-of-plane spins in BLG supported on a TMD substrate, i.e., tungsten disulfide (WS_2). We inject and detect the out-of-plane spins in graphene via a purely electrical method by exploiting the magnetic shape anisotropy of the ferromagnetic electrodes at high magnetic fields³⁴⁻³⁶, in contrast with the optical injection of out-of-plane spins into Gr/TMD systems in Refs.^{37,38}. We extract $\tau_{\perp} \approx 1$ ns-2 ns, which results in $\eta = \frac{\tau_{\parallel}}{\tau_{\perp}} \approx 40-70$ via two independent methods: Hanle measurements at high perpendicular magnetic field and a newly developed tool *oblique spin valve* measurements. Such large η confirms the existence of strong spin-valley coupling for the out-of-plane spins in BLG/TMD systems. We find a weak modulation in both τ_{\parallel} and τ_{\perp} as a function of charge carrier density in the electron-doped regime in the BLG. τ_{\parallel} varies from 15-30 ps, with such short values indicating the presence of a very strong spin-orbit coupling in

the BLG, induced by the WS₂ substrate.

7.2 Device fabrication and measurements

Bilayer-graphene/WS₂ samples are prepared on a SiO₂/Si substrate (thickness $t_{\text{SiO}_2} \approx 500$ nm) via a dry pick-up transfer method³⁹ (see the Supplemental Material⁴⁰ for fabrication details).

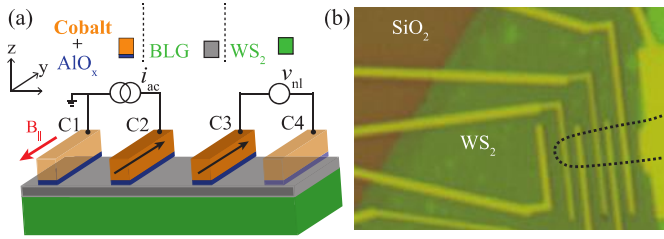


Figure 7.2-1 (a) Nonlocal spin-transport measurement scheme. The ferromagnetic electrodes C2-C3 are premagnetised along the y-axis by applying an in-plane magnetic field. The outer electrodes C1 and C4 act as reference electrodes. (b) An optical image of a part of WS₂/BLG sample (stack A) where the measurements are performed. The BLG is outlined with a black dashed line which extends further to the right.

We study two bottom-WS₂/BLG samples (thickness $t_{\text{WS}_2} \approx 3$ nm), labelled as stack A and stack B, and present the data from the left region of stack A (Figure 7.2-1 (b)) as a representative sample, i.e., the graphene region on WS₂ not covered with the hBN flake from the top. Additional measurements from stack B and the right-side region of stack A are presented in the Supplemental Material, and they also show similar results. We use a low-frequency ac lock-in detection method to measure the charge and spin transport properties of the graphene flake. In order to measure the I-V behaviour of the bottom WS₂ flake and for gate-voltage application, a Keithley 2410 dc voltage source was used. All measurements are performed at Helium temperature (4 K) under vacuum conditions in a cryostat.

Details of charge and spin-transport measurement methods⁴¹⁻⁴³ and TMD characterisation are provided in the Supplemental Material. We obtain the BLG electron-mobility $\mu_e \approx 3,000$ cm²V⁻¹s⁻¹, which is somewhat low compared to the previously reported mobility values in graphene on a TMD substrate^{1,3}.

We perform spin-transport measurements, using the measurement scheme shown in Figure 7.2-1 (a) and measure the nonlocal signal $R_{nl} = V_{NL}/i_{ac}$ as a function of magnetic field. For in-plane spin transport, the spin-signal is defined as $R_{nl}^{\parallel} = \frac{R_{nl}^{P1} - R_{nl}^{AP}}{2}$, where $R_{nl}^{AP(P)}$ is the R_{nl} measured for the (anti-)parallel magnetisation orientations of the injector-detector electrodes. From nonlocal spin-valve (SV) and Hanle spin-precession measurements, we obtain the spin diffusion coefficient D_s and in-plane spin-relaxation time τ_1 , and estimate the spin-relaxation length $\lambda_s^{\parallel} = \sqrt{D_s \tau_1}$. A representative Hanle measurement for stack A is shown in Figure 7.3-1 (b). The fitting procedure is described in the Supplemental Material. Due to small magnitudes of in-plane spin signals and invasive ferromagnetic (FM) contacts (~ 1 k Ω), we

are able to get information about the in-plane spins via Hanle measurements only for short injector-detector separation of about 1-2 μm . Since we could not access the hole-doped regime for the applied back-gate voltage in the range +40 V to -45 V due to heavily n-doped samples, we only measure the spin-transport in the electron-doped regime for both stacks. For stack A, we obtain $D_s \geq 0.01 \text{ m}^2\text{s}^{-1}$ and τ_1 in the range 18-24 ps, i.e., $\lambda_s^{\parallel} \approx 0.45\text{-}0.54 \mu\text{m}$. For stack B, we obtain $D_s \approx 0.03 \text{ m}^2\text{s}^{-1}$ and τ_1 in the range 17-24 ps, i.e., $\lambda_s^{\parallel} \approx 0.6\text{-}0.7 \mu\text{m}$. In conclusion, though for both samples we obtain reasonable charge transport properties, i.e., $D_s \approx 0.01 \text{ m}^2\text{s}^{-1}$, we obtain a very low τ_1 values. The weak modulation of τ_1 with the back-gate voltage suggests a strong SOC induced in the BLG in contact with WS_2^1 and the insignificant contribution of the spin-absorption mechanism for the applied back-gate voltage range in contrast with the behaviour observed in Refs.^{32,44,45}.

7.3 Results and discussion

A. Spin lifetime anisotropy: Hanle measurements

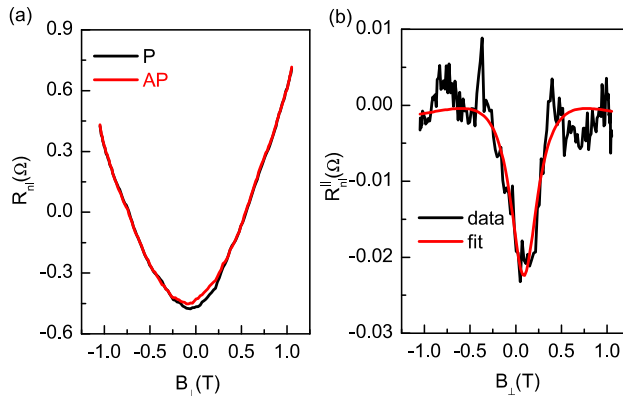


Figure 7.3-1 (a) Parallel (P) and anti-parallel (AP) Hanle curves for $L = 1 \mu\text{m}$ ($V_{\text{bg}} = 0 \text{ V}$) show a strong increase in the nonlocal resistance with the applied out-of-plane magnetic field B_{\perp} , which indicates a large spin-relaxation anisotropy and the high spin-relaxation time for the out-of-plane spins. Signs of P and AP configurations are reversed because one electrode has a negative contact polarisation for in-plane spins. (b) The Hanle spin signal R_{nl}^{\parallel} and the fit result in low $\tau_1 \approx 30\text{ps}$ (stack A).

In order to explore the proposed spin-relaxation anisotropy in BLG/ WS_2 systems²³, we inject out-of-plane spins electrically by controlling the magnetisation direction of the FM electrodes via an external magnetic field. Due to its finite shape anisotropy along the z-axis, the magnetisation of the FM electrode does not stay in the device plane at high enough B_{\perp} ^{46,47}. For the FM electrodes with the thickness $\sim 65 \text{ nm}$, their magnetisation can be aligned fully in the out-of-plane direction at $B_{\perp} \approx 1.5 \text{ T}$ ^{5,34}. At $B_{\perp} \geq 0.3 \text{ T}$, the magnetisation makes an angle $\theta > 10^\circ$ with the easy axis of the FM electrode, which increases with the field (see the Supplemental Material⁴⁰ for details). In this case, the injected spins, along with the dephasing in-plane spin-signal component as shown in Figure 7.3-1 (b) also has a nonprecessing out-of-plane spin-signal component, which would increase with B_{\perp} due to the contact

magnetisation aligning towards B_{\perp} (Figure 7.3-1 (a)). From this measurement, we can estimate τ_{\perp} by removing the contribution of the in-plane spin signal and the background charge (magneto)resistance, i.e., $R_{sq}(B_{\perp})$ (for details, refer to the Supplemental Material) and fit R_{nl} with the following equation:

$$R_{nl}(B_{\perp}) = \frac{P^2 R_{sq} \lambda_s^{\perp} e^{-\frac{L}{\lambda_s^{\perp}} (\sin \theta)^2}}{2w} \quad \text{Equation 7.3-1}$$

where $R_{nl}(B_{\perp})$ is the measured signal for out-of-plane spins for the injector-detector separation L , channel width w , with out-of-plane spin relaxation length λ_s^{\perp} . R_{sq} is the graphene sheet resistance at $B_{\perp} = 0$ T. We assume that both electrodes has equal spin-injection and detection polarisation P , which we obtain in the range 3-5% via regular in-plane spin-transport measurements (see the Supplemental Material⁴⁰ for details).

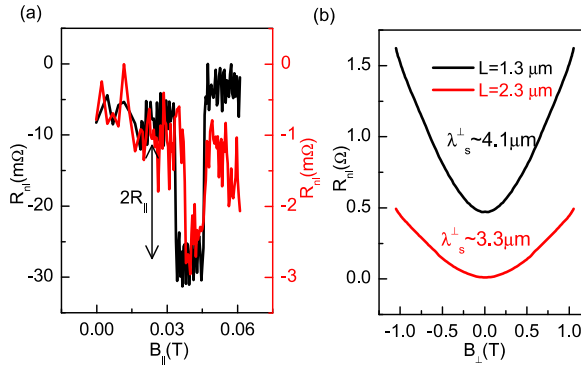


Figure 7.3-2 (a) In-plane SV signals at the injector-detector separation $L = 1.3 \mu\text{m}$ (black) and $2.3 \mu\text{m}$ (red) with their values on the left and right axis, respectively. A background signal of 0.5Ω ($7 \text{ m}\Omega$) which corresponds to Hanle signal at $B_{\perp} = 0$ T in Figure 7.3-2 (b) has been subtracted from the measured spin signal at $L = 1.3(2.3) \mu\text{m}$ for a clear representation. (b) Measured and symmetrised Hanle curves for the same L values for the parallel configuration of FM electrodes.

BLG on TMD is expected²³ to have $\tau_{\perp} \gg \tau_{\parallel}$, which also implies that $R_{nl}(B_{\perp})$ at $\theta = \pi/2$, i.e., R_{nl}^{\perp} will be higher in magnitude than R_{nl}^{\parallel} at $B_{\perp} = 0$ T. In our measurements, this effect reflects as a strong increase in R_{nl} at high B_{\perp} for both P and AP configurations (Figure 7.3-1 (a)). Via charge magnetoresistance measurements (see the Supplemental Material) for the same channel, we confirm that the observed enhancement in R_{nl} is not due to the magnetoresistance originating from the orbital effects under the applied out-of-plane magnetic field. Next, we show the distance dependence of R_{nl} in Figure 7.3-2. The in-plane spin signal R_{nl}^{\parallel} is reduced almost by factor of ten from $10 \text{ m}\Omega$ to $1 \text{ m}\Omega$ (Figure 7.3-2 (a)). On the other hand, $R_{nl}(B_{\perp})$ for the same distance decreases roughly by less than a factor of three for the entire range of B_{\perp} , which is evident from the ratio of $R_{nl}(B_{\perp})$ in black and red curves in Figure 7.3-2 (b). From this measurement, we confirm that $\tau_{\perp} \gg \tau_{\parallel}$ in the BLG/ WS_2

heterostructures. We fit the experimental data in Figure 7.3-2 (b) with Equation 7.3-1 for different L , and obtain $\lambda_s^\perp \approx 3.3 \mu\text{m} - 4.1 \mu\text{m}$. We extract τ_\perp from the relation $\lambda_s^\perp = \sqrt{D_s \tau_\perp}$, while we assume equal D_s for in-plane and out-of-plane spins³², and obtain $\tau_\perp \approx 1 \text{ ns} - 1.6 \text{ ns}$, resulting in a large anisotropy $\eta \approx 50-70$.

B. Oblique spin-valve measurements

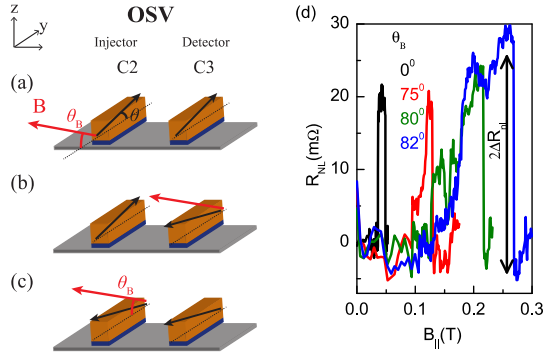


Figure 7.3 (a)-(c) Steps for oblique spin-valve (OSV) measurements. The magnetisation vector for the injector and detector (in black) makes an angle θ with the easy axis and the applied magnetic field B (red vector) for the magnetisation reversal remains fixed at an angle θ_B throughout the measurement. The magnetisation reversal for the detector and the injector are shown in (b) and (c), respectively. (d) OSV measurements at different θ_B values for the injector-detector separation $L = 1 \mu\text{m}$. Due to the negative spin polarisation of one electrode, R_{AP} is higher in magnitude than R_P . The OSV spin-signal ΔR_{nl} is defined as half of the magnitude of the switch, labeled with the black arrow. The increase in the spin-valve signal magnitude at higher θ_B confirms the presence of a large spin-relaxation anisotropy. A background signal ($\sim 0.5-1 \Omega$) has been removed from the measured signal for a clear representation (see the Supplemental Material⁴⁰ for the original measurement).

In order to confirm the spin life-time anisotropy in BLG/WS₂ system and to accurately measure the out-of-plane spin signals even in the possible presence of a background charge-signal, we develop a new tool: *oblique spin-valve* (OSV) measurements. For the OSV measurements, we follow a similar measurement procedure as in the SV measurements. However, for the magnetization reversal of FM electrodes, we apply a magnetic field B which makes an angle θ_B with their easy-axes in the y - z plane as shown in Figure 7.3-3 (a), instead of applying B_\parallel in SV measurements in Figure 7.2-1 (a). As a result, the magnetisation of the FM electrodes also makes a finite angle θ with its easy axis. In this way, we inject and detect both in-plane and out-of-plane spins in the spin-transport channel. The in-plane magnetic field $\sim B \cos(\theta_B)$ is responsible for the magnetisation switching of C2 and C3 (see details in the Supplemental Material). At the event of magnetisation reversal at a magnetic field in the OSV measurements, the spin-signal change would appear as a sharp switch in R_{nl} . However, the magnetic field dependent background signal does not change. In this way, in the OSV measurements, we combine the advantages of both SV and the perpendicular-field Hanle measurements and obtain background-free pure spin -signals. Previously reported methods^{9,32} strongly rely on the fact that there is a negligible magnetic-field dependent background present with the spin signal, and the analysis is based on Hanle spin precession and dephasing. In a stark difference, the presented OSV method is based on the spin-valve

effect where we can directly probe background-free pure spin signals and study the present spin-lifetime anisotropy in such systems.

In an OSV measurement, we measure fractions of both R_{nl}^{\parallel} and R_{nl}^{\perp} . The OSV spin-signal ΔR_{nl} consists of two components: an in-plane spin-signal component proportional to $R_{nl}^{\parallel} (\cos \theta)^2$ and an out-of-plane spin-signal component proportional to $R_{nl}^{\perp} (\sin \theta)^2$ which get dephased by the applied magnetic field $B \sin \theta_B$ and $B \cos \theta_B$, respectively:

$$\Delta R_{nl} \simeq R_{nl}^{\parallel} (\cos \theta)^2 \zeta_{\parallel} (B \sin \theta_B) + R_{nl}^{\perp} (\sin \theta)^2 \zeta_{\perp} (B \cos \theta_B) \quad \text{Equation 7.3-2}$$

where $\zeta_{\parallel(\perp)}$ is the functional form for the in-plane (out-of-plane) spin precession dynamics. At larger θ_B , the dephasing of in-plane spin-signal R_{nl}^{\parallel} is enhanced. Conversely, the dephasing of out-of-plane spin-signal R_{nl}^{\perp} is suppressed. Also, θ increases with θ_B . Therefore, ΔR_{nl} at higher θ_B is dominated by R_{nl}^{\perp} and acquires a similar form as in Equation 7.3-1.

Due to the expected spin-life time anisotropy in BLG/TMD systems and as observed in Hanle measurements in Figure 7.3-2 (b), the out-of-plane spin signal magnitude increases with the magnetisation angle θ . Similar effect would appear in the OSV measurements at larger θ_B values due to fact that the magnetisation switching would occur at larger θ , which would allow us to measure a larger fraction of the out-of-plane spin signal. In order to verify our hypothesis, we first measure the in-plane spin-valve signal $\Delta R_{nl} = R_{nl}^{\parallel}$ at $\theta_B = 0^\circ$ for $L=1 \mu\text{m}$, and then measure R_{nl} at different θ_B values. The measurement summary is presented in Figure 7.3-3 (d). Here, we clearly observe an increase in ΔR_{nl} up to 1.5 times with the increasing θ_B . This result is remarkable in the way that it is possible to observe such clear enhancement even with a small fraction of R_{nl}^{\perp} , i.e., $\alpha R_{nl}^{\perp} (\sin \theta)^2$ contributing to ΔR_{nl} . Note that, following Equation 7.3-2, for $\eta \leq 1$ (or $R_{nl}^{\perp} \leq R_{nl}^{\parallel}$), we would never observe an increase in R_{nl} . Therefore the observation of an enhanced signal in the OSV measurements is the confirmation of the present large spin life-time anisotropy in the BLG/WS₂ system.

In order to simplify the analysis and to estimate R_{nl}^{\perp} from the OSV measurements, we assume that the out-of-plane signal is not significantly affected by the in-plane magnetic field component (~ 10 mT) at $\theta_B > 80^\circ$, and $\zeta_{\perp} (B \cos \theta_B)$ can be omitted from Equation 7.3-2. Note that this assumption would lead to the lower bound of R_{nl}^{\perp} or τ_{\perp} . R_{nl}^{\parallel} and ζ_{\parallel} are obtained via the in-plane SV and Hanle spin-precession measurements (for details refer to the Supplemental Material). From R_{nl}^{\parallel} , we obtain $\lambda_s^{\perp} \approx 3.7 - 4 \mu\text{m}$, which is similar to λ_s^{\perp} obtained via Hanle measurements, and confirms the validity of the analysis. Using $\lambda_s^{\perp} = \sqrt{D_s \tau_{\perp}}$, we estimate $\tau_{\perp} \sim 1-2$ ns and the lower limit of $\eta \approx 70$ for V_{bg} between -45 V to 40 V except at $V_{bg} = -20$ V (Figure 7.3-4 (a)). Such high magnitude of $\tau_{\perp} \approx 1$ ns is also expected theoretically even in presence of spin-orbit coupling²³, which is comparable to the spin relaxation times observed in ultraclean graphene^{5,48-50}, and is a clear signature of strong spin-valley coupling present in the BLG/ WS₂ system (see the Supplemental Material⁴⁰ for additional

measurements).

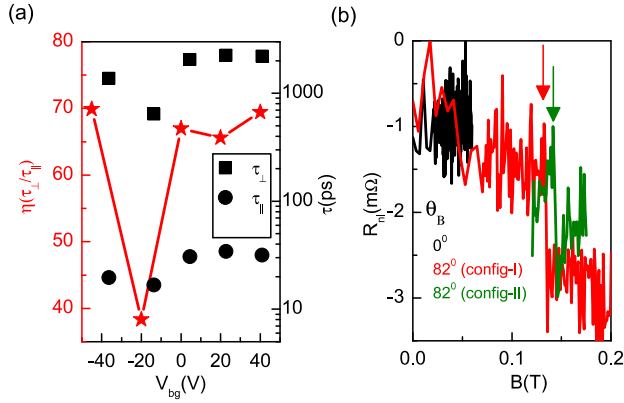


Figure 7.3-4 (a) $\eta - V_{bg}$ plot (in red) on the left y axis, and respective τ_1 and τ_{\perp} as a function V_{bg} on the right y axis (b) OSV measurements at $L = 4.3 \mu\text{m}$ at $\theta_B = 0^\circ$ (black curve), $\theta_B = 82^\circ$ (config.-I) and for the swapped injector-detector (config.-II) at $\theta_B = 82^\circ$. Arrows in the figure indicate the switching of electrode C2 in Figure 7.3-3.

In the presence of large η values in BLG/WS₂ heterostructures, the out-of-plane spin signal can still be detected at larger distances via OSV measurements whereas the in-plane is not even possible to detect. We present such a case in Figure 7.3-4 (b) for $L = 4.3 \mu\text{m}$, where no in-plane spin-signal is detected. However, we clearly measure $\Delta R_{nl} = 1.5 \text{ m}\Omega$ for $\theta_B = 82^\circ$, and obtain a similar result by swapping the injector and detector electrodes. The presented measurement unambiguously establishes the fact that indeed due to extremely large η , even though we measure a small fraction $\sim R_{nl}^{\perp} (\sin \theta)^2$ of R_{nl}^{\perp} , its magnitude is larger than the in-plane spin signal.

7.4 Conclusion

In summary, we report the first spin-transport measurements on a bilayer-graphene/TMD system. We find low in-plane spin relaxation times in the range of 20-40 ps which weakly depend on the carrier density and conductivity of the underlying TMD and therefore suggest a strong proximity induced spin-orbit coupling in the BLG. Via Hanle and OSV measurements, we electrically inject and detect out-of-plane spins in the BLG/WS₂ system. We estimate the out-of-plane spin relaxation time $\sim 1\text{-}2 \text{ ns}$ and the anisotropy value between 40-70. The possible origin of lower value could have multiple reasons, such as relative crystallographic alignment of BLG and TMD lattices, which affects the valley-Zeeman type SOC, the cleanliness and interaction between the two layers, and the doping of individual layers. We do not have a direct experimental control over these parameters. It is noteworthy that obtained η and τ_{\perp} for BLG/TMD are much larger compared to previously reported values in Gr/TMD systems in Refs.^{9,32}. These results confirm the theoretical prediction that the BLG/TMD systems are highly anisotropic and show efficient spin-valley coupling for out-of-plane spins. Obtained results unlock the potential of graphene/TMD system and confirm that the spin-lifetime anisotropy is a generic phenomenon to these heterostructures which is not limited to only single-layer graphene and thicker TMDs. These findings would be crucial

in developing future spintronic devices such as efficient spin filters and spin field-effect transistors.

7.5 Supplementary information

7.5.1 Sample preparation

Tungsten disulfide (WS_2) flakes are exfoliated on a polydimethylsiloxane (PDMS) stamp and identified using an optical microscope. The desired flake is transferred onto a pre-cleaned SiO_2/Si substrate ($t_{\text{SiO}_2} = 500 \text{ nm}$), using a transfer-stage. The transferred flake on SiO_2 is annealed in an Ar- H_2 environment at 240C for 6 hours in order to achieve a clean top-interface of WS_2 , to be contacted with graphene. The graphene flake is exfoliated from a ZYB grade HOPG (Highly oriented pyrolytic graphite) crystal and boron nitride (BN) is exfoliated from BN crystals (size $\sim 1 \text{ mm}$) onto different SiO_2/Si substrates ($t_{\text{SiO}_2} = 90 \text{ nm}$). Both crystals were obtained from HQ Graphene. The desired bilayer-graphene (BLG) flakes are identified via their optical contrast using an optical microscope. Boron-nitride flakes are identified via the optical microscope. The thickness of hBN and WS_2 flakes is determined via Atomic Force Microscopy. In order to prepare an hBN/Gr/ WS_2 stack, we use a polycarbonate (PC) film attached to a PDMS stamp as a sacrificial layer. Finally, the stack is annealed again in the Ar- H_2 environment for six hours at 235C to remove the remaining PC polymer residues.

In order to define contacts, a poly-methyl methacrylate (PMMA) solution is spin-coated over the stack and the contacts are defined via the electron-beam lithography (EBL). The PMMA polymer exposed via the electron beam gets dissolved in a MIBK:IPA (1:3) solution. In the next step, 0.7 nm Al is deposited in two steps, each step of 0.35 nm followed by 12 minutes oxidation in the oxygen rich environment to form a AlO_x tunnel barrier. On top of it, 65 nm thick cobalt (Co) is deposited to form the ferromagnetic (FM) tunnel contacts with a 3 nm thick Al capping layer to prevent the oxidation of Co electrodes. The residual metal on the polymer is removed by the lift-off process in acetone solution at 40 °C.

7.5.2 Charge transport measurements

7.5.2.1 Graphene

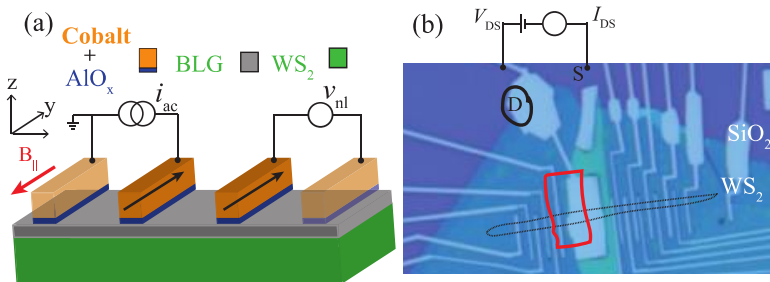


Figure 7.5-1 (a) Nonlocal spin-transport measurement scheme. (b) An optical micrograph of a fabricated $\text{WS}_2/\text{BLG}/\text{hBN}$ stack (stack A). BLG is outlined with black dashed lines and hBN top-gate is outlined in red.

We measure the charge transport in graphene via the four-probe local measurement scheme. For measuring the gate-dependent resistance of graphene-on-WS₂, a fixed ac current $i_{ac} \approx 100$ nA is applied between contacts C1-C4 and the voltage-drop is measured between contacts C2-C3 (Figure 7.5-1 (a)), while the back-gate voltage is swept. The maximum resistance point in the Dirac curve is denoted as the charge neutrality point (CNP). For graphene-on-WS₂, it is possible to tune the Fermi energy E_F and the carrier-density in graphene only when E_F lies only in the band-gap of WS₂. Since, we do not observe any saturation in the resistance of the BLG (red curve Figure 7.5-2 (a)), we probe the charge/ spin transport where the Fermi level lies within the band gap of WS₂. The CNP cannot be accessed within the applied V_{bg} range. However, it is possible to access the CNP and the hole doped regime (black curves Figure 7.5-2 (a)) in the region underneath the top-hBN flake, outlined as red region in the optical image in Figure 7.5-1 (b), using the top-gate application due to its higher capacitance.

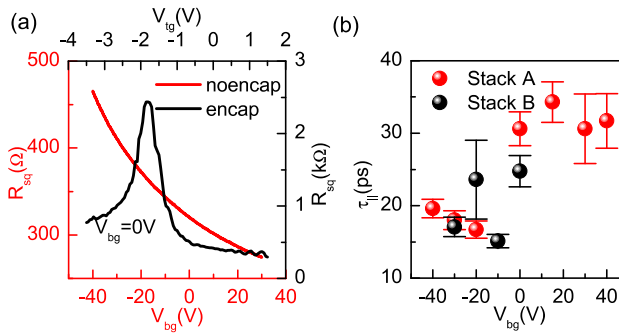


Figure 7.5-2 (a) $R_{sq} - V_{bg(rg)}$ dependence for the nonencapsulated (encapsulated) region is shown on the left (right) axis (red(black) curves) for stack A. (b) $\tau_1 - V_{bg}$ for BLG/ WS₂.

In order to extract the carrier mobility μ , we fit the charge-conductivity σ versus carrier density n plot with the following equation:

$$\sigma = \frac{1}{R_{sq}} = \frac{ne\mu + \sigma_0}{1 + R_S(ne\mu + \sigma_0)} \quad \text{Equation 7.5-1}$$

where R_{sq} is the square resistance of graphene, σ_0 is the conductivity at the CNP, R_{sq} is the residual resistance due to short-range scattering^{39,41} and e is the electronic charge. We fit the $\sigma - n$ data for n (both electrons and holes) in the range $0.5 - 2.5 \times 10^{12} \text{ cm}^{-2}$ with Equation 7.5-1. For the encapsulated region we obtain the electron-mobility $\mu_e \approx 3,000 \text{ cm}^2 \text{ V}^{-1} \text{ s}^{-1}$ for stack A. For stack B, we could not access the CNP within the applied V_{bg} range due to heavily n-doped BLG. Therefore, we could not extract the mobility.

Diffusion coefficient of graphene can be extracted from the $\sigma - n$ dependence using the Einstein relationship:

$$D_c = \frac{\sigma}{e^2 v(E)} \quad \text{Equation 7.5-2}$$

where D_c is the charge diffusion coefficient, e is the electronic charge, and $v(E)$ is the density

of states of the BLG at energy E . The total number of carriers n can be calculated using the relation:

$$n = \int_0^{E_F} v(E) dE \quad \text{Equation 7.5-3}$$

$v(E)$ of the BLG is:

$$v(E) = \frac{g_s g_v}{4\pi\hbar^2 v_F^2} (2E + \gamma_1) \quad \text{Equation 7.5-4}$$

where g_s and g_v are electron spin and valley degeneracy ($=2$), \hbar is the reduced Planck coefficient, $v_F = 106$ m/s is the electron Fermi velocity, and $\gamma_1 = 0.37$ eV is the interlayer coupling coefficient.

In order to account for the broadening of the density of states near the charge neutrality point, Equation 7.5-4 can be rewritten as:

$$v(E) = \frac{g_s g_v}{2\pi\hbar^2 v_F^2} \left(\frac{2b}{\sqrt{2\pi}} \exp\left(-\frac{E^2}{2b^2}\right) + E \times \text{erf}\left(\frac{E}{b\sqrt{2}}\right) + 0.5\gamma_1 \right). \quad \text{Equation 7.5-5}$$

Here $b = 75$ meV is the Gaussian broadening energy and erf is the Gaussian error function. By solving Equation 7.5-5 and Equation 7.5-3, we can obtain E and calculate $v(E)$. Now, using the relation in Equation 7.5-2, we obtain $D_c \approx 0.01$ m²s⁻¹ for the hBN encapsulated region.

7.5.2.2 Tungsten disulfide (WS₂)

In order to obtain the transfer characteristics, i.e., back-gate dependent conductivity of the WS₂ substrate, we apply a dc voltage $V_{DS} = 0.2$ V and measured the current I_{DS} between the top gate contact, that touches the bottom WS₂ at point D and a contact S on the BLG flake (Figure 7.5-1 (b)), and vary the back-gate voltage V_{bg} in order to change the resistivity of WS₂. The $I_{DS} - V_{bg}$ behaviour of the bottom-WS₂ flake of stack A is plotted in Figure 7.5-3.

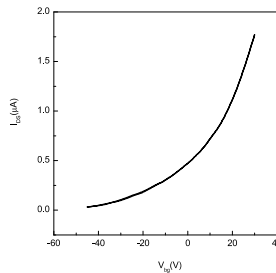


Figure 7.5-3 $I_{DS} - V_{bg}$ behavior of the bottom-WS₂ flake of stack A at $V_{DS} = 0.2$ V applied between the top-gate electrode and another electrode contacting the BLG-on-WS₂. The measurement scheme is shown in Figure 7.5-1(b).

7.5.3 Spin transport measurements

For spin-valve (SV) measurements, a charge current i_{ac} is applied between contacts C2-C1 and a nonlocal voltage V_{NL} is measured between C3-C4 (Figure 7.5-1 (a)). First an in-plane magnetic field $B_1 \approx 0.2$ T is applied along the easy axes of the ferromagnetic (FM) electrodes (+y-axis), in order to align their magnetisation along the field. Now, B_1 is swept in the opposite direction (-y-axis) and the FM contacts reverse their magnetisation direction along the applied field, one at a time. This magnetisation reversal appears as a sharp transition in V_{NL} or in the nonlocal resistance $R_{nl} = V_{NL}/i_{ac}$. The spin-signal is $R_{nl}^{\parallel} = \frac{R_{nl}^P - R_{nl}^{AP}}{2}$, where $R_{nl}^{P(AP)}$ represents the R_{nl} value of the two level spin-valve signal, corresponding to the parallel (P) and anti-parallel (AP) magnetisation of the FM electrodes. In the nonlocal measurement geometry the spin-signal R_{nl}^{\parallel} is given by:

$$R_{nl}^{\parallel} = \frac{P^2 R_{sq} \lambda_s^{\parallel} e^{-\frac{L}{\lambda_s^{\parallel}}}}{2w} \quad \text{Equation 7.5-6}$$

where λ_s^{\parallel} is the spin-relaxation length for the in-plane spins in graphene and P is the contact polarisation of injector and detector electrodes for in-plane spins, R_{sq} is the graphene sheet-resistance and w is the width of spin-transport channel.

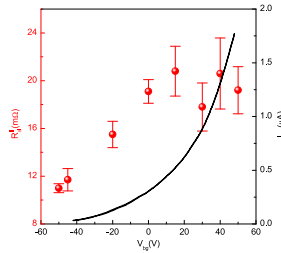


Figure 7.5-4 In-plane Spin valve (SV) measurements for stack A as a function of V_{bg} and the conductance of the underlying TMD (WS_2).

For Hanle spin-precession measurements^{3,42}, for a fixed P (AP) configuration, an out-of-plane magnetic field B_L is applied and the injected in-plane spin-accumulation precesses around the applied field. From these measurements, we obtain the spin diffusion coefficient D_s and in-plane spin-relaxation time τ_1 . The measured Hanle curves are fitted with the steady state solution to the one dimensional Bloch equation:

$$D_s \nabla^2 \mu_s^{\vec{}} - \frac{\mu_s^{\vec{}}}{\tau_s} + \omega_L X \mu_s^{\vec{}} = 0 \quad \text{Equation 7.5-7}$$

with the spin diffusion constant D_s , spin relaxation time τ_s and spin-accumulation $\mu_s^{\vec{}}$ in the transport channel. The spin diffusion length $\lambda_s = \sqrt{D_s \tau_s}$. The obtained D_s from the Hanle

precession measurements $0.01 - 0.02 \text{ m}^2\text{s}^{-1}$, which is of similar magnitude of the diffusion coefficient obtained from the charge transport measurements, and establishes the validity of the analysis.

Using this λ_s^{\parallel} in Equation 7.5-6, we obtain the contact polarisation $P \approx 3-5 \%$ for in-plane spin-transport. We would like to make a remark here that some of the contacts in stack A have the opposite (i.e., negative) sign of P for in-plane spin-transport. The origin of the negative sign is nontrivial and possibly could be due to the specific nature of the FM tunnel barrier interface with the graphene-on-TMD.

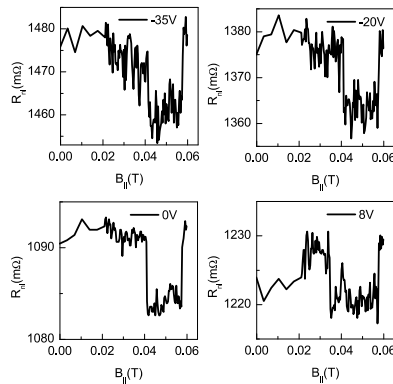


Figure 7.5-5 In-plane Spin valve (SV) measurements for stack B at different back-gate voltage (V_{bg}) values. R_{nl}^{\parallel} does not change with V_{bg} , indicating that the spin-absorption is not the dominant mechanism for spin-relaxation within the applied V_{bg} range.

SV measurements as a function of V_{bg} (stack B) are summarized in Figure 7.5-4 and Figure 7.5-5 for stack A and stack B, respectively. For both samples, there is no significant change in the spin-signal within the range $\Delta V_{bg} \approx \pm 40\text{V}$. For stack A, the FM contacts have low resistance ($\leq 1\text{k}\Omega$) and this is the reason that there is a modest increase in R_{nl}^{\parallel} at higher charge carrier density due to the suppressed contact-induced spin-relaxation^{26,43}. Both measurements do not exhibit any measurable signature of spin-absorption due to the conductivity modulation of the underlying TMD substrate.

7.5.4 Generalised Stoner-Wohlfarth Model for extracting magnetisation angle

In this section, we describe the basics of Stoner-Wohlfarth (SW) model, and extend it for three dimensional case in order to extract the magnetisation-direction of a bar-magnet in presence of an external magnetic field.

The total energy E_T of a ferromagnet in a magnetic field is expressed as:

$$E_T = E_A + E_Z$$

Equation 7.5-8

where E_Z and E_A are the contributions from Zeeman and anisotropic energy, respectively.

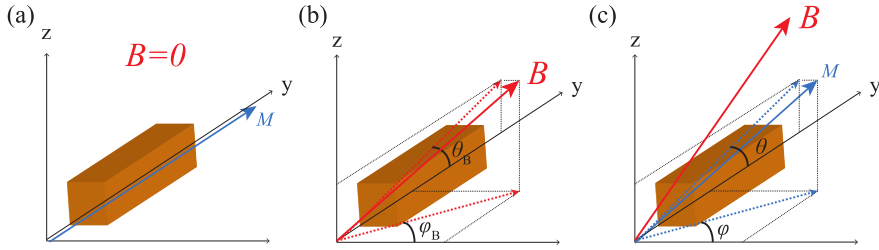


Figure 7.5-6 Easy axis of magnetisation M for the bar magnet is along its length, i.e., along y -axis. (a) M is along y -axis for $B = 0$ or when B is applied along y -axis. (b) For $B \neq 0$ T, M makes an angle θ with the x - y plane and angle ϕ with the y - z plane and (c) B makes an angle θ_B with the x - y plane and angle ϕ_B with the y - z plane.

First a magnetic field B is applied which makes an angle ϕ_B with the x -axis and an angle θ_B (Figure 7.5-6 (b)), having its components B_x, B_y, B_z along x, y and z axes, respectively. Here B can be parameterized with respect to θ_B, ϕ_B in the following way:

$$B_x = B \cos \theta_B \cos \phi_B, B_y = B \cos \theta_B \sin \phi_B, B_z = B \sin \theta_B. \quad \text{Equation 7.5-9}$$

For a ferromagnetic bar with its anisotropic constants K_x, K_y and K_z along x, y and z axes respectively, and \vec{M} making an angle α_x, α_y and α_z with the x, y and z axes respectively, E_T be generalised to a three-dimensional form as:

$$E_T = \sum_{i=x,y,z} E_A^i + \sum_{i=x,y,z} E_Z^i. \quad \text{Equation 7.5-10}$$

Now we write down the expression for E_A^i and E_Z^i which have contributions from M_i and B_i .

At (B, θ_B, ϕ_B) \vec{M} makes the azimuthal angle ϕ with the x -axis in the x - y plane and polar angle θ with the y -axis in the y - z plane (Figure 7.5-6 (c)). Therefore, $\vec{M} = (M_x, M_y, M_z) = (M \cos \theta \cos \phi, M \cos \theta \sin \phi, M \sin \theta)$. The anisotropic and Zeeman energy terms can again be parameterised with respect to $\theta, \phi, \theta_B, \phi_B$ in to a three-dimensional form:

$$\begin{aligned} E_A^x &= K_x (\sin \alpha_x)^2 = K_x (1 - (\cos \theta)^2 (\cos \phi)^2), \\ E_A^y &= K_y (\sin \alpha_y)^2 = K_y (1 - (\cos \theta)^2 (\sin \phi)^2), \\ E_A^z &= K_z (\sin \alpha_z)^2 = K_x (\cos \theta)^2 \end{aligned} \quad \text{Equation 7.5-11}$$

and

$$E_Z^x = -M_x B_x,$$

$$E_Z^y = -M_y B_y,$$

$$E_z^Z = -M_z B_z.$$

Equation 7.5-12

Now the expressions in Equation 7.5-11 and Equation 7.5-12 can be substituted to Equation 7.5-10 and a full functional form of E_T can be obtained.

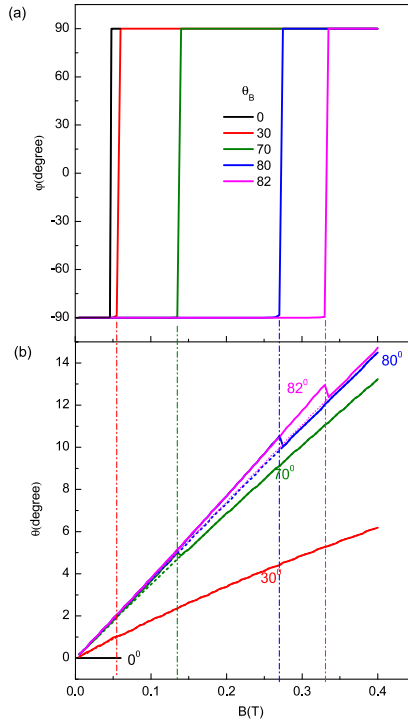


Figure 7.5-7 (a) in-plane ϕ and (b) out-of-plane θ angles as a function of magnetic field at different θ_b values. Dashed lines in the θ - B plot correspond to the situation when B and M have their in-plane components in the same direction in the y - z plane. Sharp switches in ϕ , θ correspond to the event when the magnetisation reversal occurs.

In order to obtain (θ, ϕ) which correspond to $\min(E_T)$, we solve for the global energy minima of Equation 7.5-10 by imposing two following conditions:

$$\frac{\partial E_T(\theta, \phi)}{\partial \theta} = \frac{\partial E_T(\theta, \phi)}{\partial \phi} = 0, \quad \frac{\partial^2 E_T(\theta, \phi)}{\partial \theta^2} = \frac{\partial^2 E_T(\theta, \phi)}{\partial \phi^2} = 0. \quad \text{Equation 7.5-13}$$

Since \vec{M} has its easy axis along y -axis, $K_y = 0$. We use $M_{cobalt} = 5 \times 10^5$ A/m as reported in literature⁴⁶. In order to obtain K_z , we use the saturation magnetic field M_s of the FM electrodes along z -direction, i.e. ~ 1.5 T for the thickness (65nm) of the FM electrodes, and use the relation⁴⁷ $M_s = \frac{k_z}{M_{cobalt}}$. In order to obtain K_x , we use the in-plane switching fields of FM electrodes, and use them as the only free parameter in the model to obtain the in-plane magnetisation switching as obtained in measurements.

Using the procedure, we numerically solve for θ , ϕ for different directions of the applied magnetic field with respect to the minimum energy constraint in Equation 7.5-13 using MATLAB. The simulation outcome is shown in Figure 7.5-7.

7.5.5 Oblique Spin-valve measurements

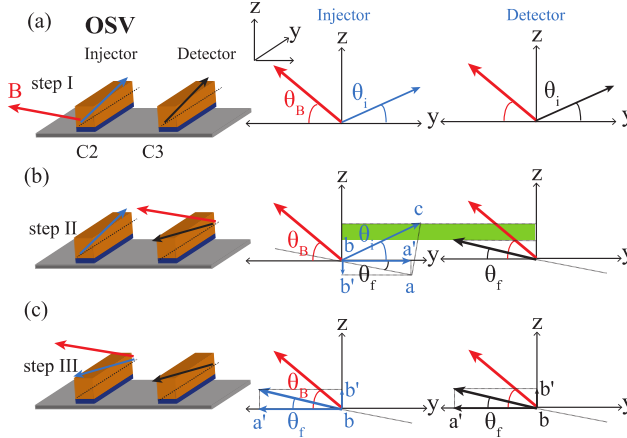


Figure 7.5-8 Steps for Oblique Spin Valve Measurements

Before starting the oblique spin-valve (OSV) measurements, we set the initial \vec{M} of the FM electrodes along $+y$ -axis, i.e. along their easy magnetisation-axis. Here, the measured spin-signal $R_{nl}^T = R_{nl}^{\parallel}$.

Step-I: We apply a magnetic field B in the opposite direction which makes an angle θ_B with the $-y$ -axis, as shown in Figure 7.5-8 (a). Here, we assume that both injector and the detector due to their identical thickness have the same out-of-plane anisotropy value K_z . As the magnitude of B increases, the magnetisation \vec{M} of both injector and detector FM electrodes makes a finite angle θ_i with respect to its initial direction ($+y$ -axis), and the injected spins have their quantisation axis along θ_i (Figure 7.5-8 (a)). Now, the measured spin-signal R_{nl}^{P1} in the parallel configuration can be expressed as:

$$R_{nl}^{P1} \simeq R_{nl}^{\parallel} (\cos \theta_i)^2 \zeta_{\parallel}(B \sin \theta_B) + R_{nl}^{\perp} (\sin \theta_i)^2 \zeta_{\perp}(B \cos \theta_B) \quad \text{Equation 7.5-14}$$

where, $\zeta_{\parallel(\perp)}$ is the functional form for the in-plane (out-of-plane) spin precession of dynamics.

Step-II: Due to different widths of the FM electrodes, they have different in-plane anisotropies and different switching fields. At a certain magnetic field, the magnetisation of the detector reverses the direction of its y -component. Now, the detector magnetisation subtends an angle θ_f with the negative y -axis (Figure 7.5-8 (b)). This activity is seen as a switch due to the direction reversal of both in-plane and out-of-plane magnetisation

component with respect to its initial orientation. The factorisation of in-plane and out-of-plane components can be understood via the presented vector diagram in Figure 7.5-8 (b) in following steps:

- The injector electrode injects the spin signal along θ_i , represented by the blue arrow b-c in Figure 7.5-8 (b).
- The detector measures the projection of the injected spin-signal which has its quantisation axis at θ_i , along the detector magnetization axis along b-a, shown as a black dashed line in Figure 7.5-8 (b). Now the magnetisation axis, along which the spin-signal is measured becomes:

$$\vec{M}_{\text{injector}}^{\text{new}} = -(\hat{j} \cos \theta_f + \hat{k} \sin \theta_f) \cos(\theta_i + \theta_f) \quad \text{Equation 7.5-15}$$

where \hat{j} , \hat{k} are the unit vectors along y and z-axis, respectively. Since the in-plane and out-of-plane spin-signals have magnitudes $R_{nl}^{\parallel} \cos \theta_i \zeta_{\parallel} (B \sin \theta_B)$ and $R_{nl}^{\perp} \sin \theta_i \zeta_{\perp} (B \cos \theta_B)$, the spin-signal measured by the detector becomes:

$$R_{nl}^{\text{AP}} = -[R_{nl}^{\parallel} \cos \theta_i \zeta_{\parallel} (B \sin \theta_B) \cos \theta_f + R_{nl}^{\perp} \sin \theta_i \zeta_{\perp} (B \cos \theta_B) \sin \theta_f] \cos(\theta_i + \theta_f). \quad \text{Equation 7.5-16}$$

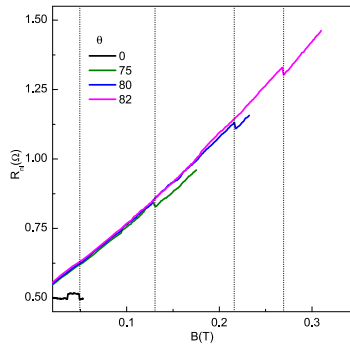


Figure 7.5-9 (a) OSV measurements for BLG/WS₂ at different θ_B values for the injector-detector separation $L=1 \mu\text{m}$ with out background removal. Vertical dashed lines indicate the magnitudes of the magnetisation switching field magnitudes on x-axis at different θ_B values. The black curve is the in-plane spin-valve measurement at $\theta_B = 0$. The curves measured at $\theta_B = 75-82^\circ$ have the contribution from both in-plane and out-of-plane spin-signals. The enhanced contribution of the out-of-plane spin-signal component during the magnetisation reversal, i.e. enhanced switch magnitude in R_{nl} for the measurements at higher θ_B values can be seen clearly in Figure 7.3-3 (b) of the main text, after the background removal.

Step-III: Finally, the injector electrode reverses its magnetisation and both electrodes have their magnetisations pointing in the same direction, and making an angle θ_f with the device plane Figure 7.5-8 (c). The spin-signal R_{nl}^{P2} has the same expression as in Equation 7.5-14, except θ_i is replaced with θ_f . The desired spin valve signal can be obtained by subtracting

Equation 7.5-16 with Equation 7.5-14 with appropriate θ values, obtained from Figure 7.5-7 at corresponding magnetisation switching fields.

A data set for the oblique spin valve measurements is shown in Figure 7.5-9. As expected by the simulation results in Figure 7.5-7, the magnetisation switching follows the relation $B_0 \approx B \cos \theta_B$, where B_0 is the magnetisation switching field ~ 40 mT for the in-plane spin valve (black curve in Figure 7.5-9). The measured signal has contribution from both in-plane and out-of-plane magnetisation switching. As suggested by the simulation results, the magnetic field dependent background in the measurement has similar trend as observed in Figure 7.5-7 (b)) due to the field-dependent magnetisation angle, and has contribution of the out-of-plane spin-signal. The processed data after removing this field dependence is shown in Figure 7.3-3 (a) of the main text which shows a clear enhancement in the measured spin valve signal magnitude. This is a consequence of large spin-life time anisotropy present in the system, and is discussed in the manuscript in detail.

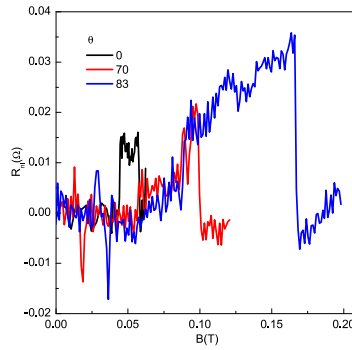


Figure 7.5-10 Additional OSV measurements at $L = 1 \mu\text{m}$ at $V_{bg} = 0$ V (stack A).

An additional set of OSV measurements for a different region (on the right side) of stack A is shown in Figure 7.5-10. For this set the FM electrodes at $\theta_B = 83^\circ$ switch earlier than the expected switching field, i.e. $B_0 / \cos \theta_B \approx 300$ mT, and using the angles obtained in Figure 7.5-7 and τ_1 in the region, the analysis yields $\eta \approx 244$ and $\tau_1 \approx 4$ ns. The overestimation of η is probably due to earlier switching of the FM electrode. However, the effect of anisotropy can be clearly seen in the measurement.

7.5.6 Nonlocal Hanle signal versus orbital magnetoresistance

A negligible charge background signal due to the orbital magnetoresistance of the graphene flake is present at the applied B_\perp as shown in Figure 7.5-11.

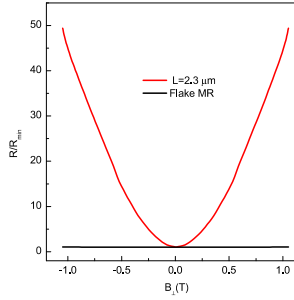


Figure 7.5-11 Hanle (parallel configuration) at the injector-detector separation $L = 2.3 \mu\text{m}$ and the flake magnetoresistance (black curve) are symmetrised and normalised with R_{nl}^{\min} and R_{MR}^{\min} value in order to emphasise the signal enhancement in the nonlocal configuration.

Here, for the same channel R_{nl} increases almost 50 fold whereas there is hardly any change in the background MR signal (Figure 7.5-11). Therefore the observed increase in R_{nl} at high B_{\perp} is clearly not due to the orbital magnetoresistance of the graphene-flake.

7.5.7 Estimating out-of-plane spin relaxation time via Hanle measurements

It is already explained in the previous section that at a nonzero magnetic field B applied at an angle θ_B with the device plane, the magnetisation vector \vec{M} makes a finite angle θ with the device plane (Figure 7.5-6). Here, we represent a specific case with $\theta_B = 90^\circ$ for Hanle measurements. Here, we would represent B as B_{\perp} and assume that both injector and detector behave identically and their \vec{M} vectors make same angle θ . At $B_{\perp} \neq 0$, \vec{M} has its quantisation axis not in the device plane, it also electrically injects a nonzero out-of-plane spin-signal. If \vec{M} for both injector and detector were pointing perpendicular to the device plane, the measured nonlocal signal R_{nl}^{\perp} would be written as:

$$R_{nl}^{\perp} = \frac{P^2 R_{sq}(B_{\perp}) \lambda_s^{\perp} e^{-\frac{L}{\lambda_s^{\perp}}}}{2w} \quad \text{Equation 7.5-17}$$

where λ_s^{\perp} is the spin-relaxation length for the out-of-plane spins in graphene and P is the contact polarisation of injector and detector electrodes, which is obtained via in-plane spin-transport measurements. $R_{sq}(B_{\perp})$ is the magnetoresistance (MR) of the graphene flake in presence of the out-of-plane magnetic field. However, in general $\theta < \pi/2$ for the values of $B_{\perp} < 1.2 \text{ T}$ due to limitations of the electromagnet in the setup, we inject and detect only a fraction of R_{nl}^{\perp} that is proportional to $(\sin \theta)^2(B_{\perp})$, and the in-plane spin-signal R_{nl}^{\parallel} that is proportional to $(\cos \theta)^2(B_{\perp})$ and gets dephased by B_{\perp} .

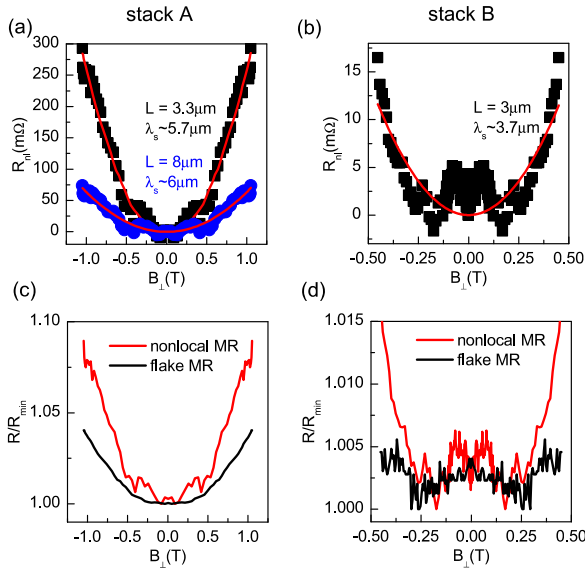


Figure 7.5-12 (a) Symmetrised Hanle curves (stack A) and fits (in red) with Equation 7.5-23 after subtracting the background-signal of $\sim 3 \Omega$ and 1Ω at two different injector-detector separations, respectively (at $V_{bg} = 0$) result in similar λ_s^\perp . (b) Additional Hanle measurements and the fit for stack B (after subtracting the background signal $\sim 1 \Omega$). Nonlocal resistance and flake magnetoresistance are normalised and plotted together in order to highlight the relative difference between them in (c) for stack A and (d) for stack B.

FM contacts also measure charge-related MR and a constant spin-independent background due to current spreading and homogeneous current distribution even in the nonlocal part of the circuit. This contribution can be represented as:

$$R_{nl}^{ch} = C1R_{sq}(B_\perp) + C2. \quad \text{Equation 7.5-18}$$

Therefore, the total measured nonlocal signal R_{nl}^T is:

$$R_{nl}^T(B_\perp) = R_{nl}^\perp (\sin \theta)^2(B_\perp) \pm R_{nl}^\parallel (\cos \theta)^2(B_\perp) \times \zeta(B_\perp) + R_{nl}^{ch}. \quad \text{Equation 7.5-19}$$

Here $+(-)$ before the expression for the in-plane spin signal is for P(AP) magnetization configuration of the injector-detector electrodes and $\zeta(B_\perp)$ is the expression for Hanle precession dynamics. The second term can be omitted from Equation 7.5-19 by measuring $R_{nl}^T(B_\perp)$ for both P and AP configurations of FM electrodes and then averaging them out. Via this exercise, we get rid of the in-plane spin signal and get the following expression:

$$R_{nl}^T(B_\perp) = R_{nl}^\perp (\sin \theta)^2(B_\perp) \pm C1R_{sq}(B_\perp) + C2. \quad \text{Equation 7.5-20}$$

At $B_\perp = 0 \text{ T}$, $R_{sq}(B_\perp = 0) = R_{sq}$ and $\theta(B_\perp = 0) = 0$, Equation 7.5-20 reduces to:

$$R_{nl}^T(0) = C1R_{sq} + C2. \quad \text{Equation 7.5-21}$$

By subtracting Equation 7.5-21 to Equation 7.5-20 and dividing the resulting expression with $R_{sq}(B_{\perp})$, we obtain:

$$\frac{R_{nl}^T(B_{\perp}) - R_{nl}^T(0)}{R_{sq}(B_{\perp})} = \frac{R_{nl}^{\perp}(\sin \theta)^2(B_{\perp})}{R_{sq}(B_{\perp})} + C1 \frac{R_{sq}(B_{\perp}) - R_{sq}}{R_{sq}(B_{\perp})}. \quad \text{Equation 7.5-22}$$

Using Equation 7.5-17, we obtain the final expression:

$$\frac{R_{nl}^T(B_{\perp}) - R_{nl}^T(0)}{R_{sq}(B_{\perp})} = \frac{p^2 \lambda_s^{\perp} e^{-\frac{L}{\lambda_s^{\perp}}} (\sin \theta)^2(B_{\perp})}{2w} + C1 \frac{R_{sq}(B_{\perp}) - R_{sq}}{R_{sq}(B_{\perp})} \quad \text{Equation 7.5-23}$$

and use it for extracting λ_s^{\perp} and the constant $C1$ which is the fraction of flake MR contributing to the nonlocal signal. Here, θ is obtained via simulations, following the procedure mentioned earlier using $\theta_B = \pi/2$. Experimental data of R_{nl} and the fit with Equation 7.5-23 is shown in Figure 7.5-12 (a,b).

7.5.8 Estimation of Valley-Zeeman and Rashba SOC strengths

In graphene/TMD heterostructures, different spin-orbit coupling strengths are induced in graphene in the in-plane and out-of-plane directions because of weak van der Waals interactions with the contacting TMD⁸. This effect can be measured in the anisotropy of in-plane τ_{\parallel} and out-of-plane spin-relaxation time τ_{\perp} using the following relation:

$$\eta = \frac{\tau_{\perp}}{\tau_{\parallel}} \approx \frac{\tau_{iv}}{\tau_p} \left(\frac{\lambda_{vZ}}{\lambda_R} \right)^2 \quad \text{Equation 7.5-24}$$

where λ_{vZ} and λ_R are spin-orbit coupling strengths corresponding to the out-of-plane and in-plane spin-orbit field, respectively. τ_{iv} is the intervalley scattering time, and τ_p is the momentum relaxation time of electron.

From the charge and spin transport measurements, we obtain the diffusion coefficient $D \approx 0.01 - 0.03 \text{ m}^2\text{V}^{-1}\text{s}^{-1}$. Following the relation $D \approx v_F^2 \tau_p$, where $v_F = 10^6 \text{ ms}^{-1}$ is the Fermi velocity of electrons in graphene, we obtain $\tau_p \approx 0.01 - 0.03 \text{ ps}$. Typically, for strong inter-valley scattering, we can assume the relation⁸ $\tau_{iv} \sim 5\tau_p$, and estimate $\tau_{iv} \approx 0.05 - 0.15 \text{ ps}$. From the spin-transport experiments, we already know $\tau_{\perp} \approx 1 \text{ ns}$ and $\tau_{\parallel} \approx 30 \text{ ps}$. We can now estimate λ_R and λ_{vZ} independently by assuming that the spin-relaxation is dominated by the Dyakonov Perel mechanism⁸, i.e. using the relations $\tau_{\perp}^{-1} = \left(\frac{2\lambda_R}{\hbar} \right)^2$ and $\tau_{\parallel}^{-1} = \left(\frac{2\lambda_{vZ}}{\hbar} \right)^2 \tau_{iv}$, respectively. We obtain $\lambda_R \sim 100 \text{ } \mu\text{eV}$ and $\lambda_{vZ} \approx 350 \text{ } \mu\text{eV}$. The obtained values are of similar order magnitude as reported in literature^{3,7,8}.

References

1. Wang, Z. et al. Origin and magnitude of ‘designer’ spin-orbit interaction in graphene on semiconducting transition metal dichalcogenides. *Phys. Rev. X* **6**, 1–15 (2016).
2. Gmitra, M. & Fabian, J. Graphene on transition-metal dichalcogenides: A platform for proximity spin-orbit physics and optospintronics. *Phys. Rev. B* **92**, 155403 (2015).
3. Omar, S. & van Wees, B. J. Spin transport in high-mobility graphene on WS₂ substrate with electric-field tunable proximity spin-orbit interaction. *Phys. Rev. B* **97**, 45414 (2018).
4. Xiao, D., Yao, W. & Niu, Q. Valley-Contrasting Physics in Graphene: Magnetic Moment and Topological Transport. *Phys. Rev. Lett.* **99**, 236809 (2007).
5. Leutenantsmeyer, J. C., Ingle-Aynés, J., Fabian, J. & van Wees, B. J. Observation of Spin-Valley-Coupling-Induced Large Spin-Lifetime Anisotropy in Bilayer Graphene. *Phys. Rev. Lett.* **121**, 127702 (2018).
6. Xu, J., Zhu, T., Luo, Y. K., Lu, Y.-M. & Kawakami, R. K. Strong and Tunable Spin-Lifetime Anisotropy in Dual-Gated Bilayer Graphene. *Phys. Rev. Lett.* **121**, 127703 (2018).
7. Zihlmann, S. et al. Large spin relaxation anisotropy and valley-Zeeman spin-orbit coupling in WSe₂/graphene/h-BN heterostructures. *Phys. Rev. B* **97**, 75434 (2018).
8. Cummings, A. W., Garcia, J. H., Fabian, J. & Roche, S. Giant Spin Lifetime Anisotropy in Graphene Induced by Proximity Effects. *Phys. Rev. Lett.* **119**, 206601 (2017).
9. Ghiasi, T. S., Ingle-Aynés, J., Kaverzin, A. A. & Van Wees, B. J. Large Proximity-Induced Spin Lifetime Anisotropy in Transition-Metal Dichalcogenide/Graphene Heterostructures. *Nano Lett.* **17**, 7528–7532 (2017).
10. Safeer, C. K. et al. Room-Temperature Spin Hall Effect in Graphene/MoS₂ van der Waals Heterostructures. *Nano Lett.* **19**, 1074–1082 (2019).
11. Garcia, J. H., Cummings, A. W. & Roche, S. Spin Hall Effect and Weak Antilocalization in Graphene/Transition Metal Dichalcogenide Heterostructures. *Nano Lett.* **17**, 5078–5083 (2017).
12. Song, Q. et al. Observation of inverse Edelstein effect in Rashba-split 2DEG between SrTiO₃ and LaAlO₃ at room temperature. *Sci. Adv.* **3**, (2017).
13. Soumyanarayanan, A., Reyren, N., Fert, A. & Panagopoulos, C. Emergent phenomena induced by spin-orbit coupling at surfaces and interfaces. *Nature* **539**, 509 (2016).
14. Isasa, M. et al. Origin of inverse Rashba-Edelstein effect detected at the Cu/Bi interface using lateral spin valves. *Phys. Rev. B* **93**, 14420 (2016).
15. Sánchez, J. C. R. et al. Spin-to-charge conversion using Rashba coupling at the interface between non-magnetic materials. *Nat. Commun.* **4**, 2944 (2013).
16. Shen, K., Vignale, G. & Raimondi, R. Microscopic Theory of the Inverse Edelstein Effect. *Phys. Rev. Lett.* **112**, 96601 (2014).
17. Kane, C. L. & Mele, E. J. Z₂ Topological Order and the Quantum Spin Hall Effect. *Phys. Rev. Lett.* **95**,

- 146802 (2005).
18. Yang, B. et al. Tunable spin-orbit coupling and symmetry-protected edge states in graphene/WS₂. *2D Mater.* **3**, 31012 (2016).
 19. Frank, T., Högl, P., Gmitra, M., Kochan, D. & Fabian, J. Protected Pseudohelical Edge States in Z₂-Trivial Proximitized Graphene. *Phys. Rev. Lett.* **120**, 156402 (2018).
 20. Du, L. et al. Robust spin-valley polarization in commensurate MoS₂/graphene heterostructures. *Phys. Rev. B* **97**, 115445 (2018).
 21. Island, J. O. et al. Spin-orbit-driven band inversion in bilayer graphene by the van der Waals proximity effect. *Nature* **571**, 85–89 (2019).
 22. Khoo, J. Y., Morpurgo, A. F. & Levitov, L. On-Demand Spin-Orbit Interaction from Which-Layer Tunability in Bilayer Graphene. *Nano Lett.* **17**, 7003–7008 (2017).
 23. Gmitra, M. & Fabian, J. Proximity Effects in Bilayer Graphene on Monolayer WSe₂: Field-Effect Spin Valley Locking, Spin-Orbit Valve, and Spin Transistor. *Phys. Rev. Lett.* **119**, 146401 (2017).
 24. Afzal, A. M. et al. Gate Modulation of the Spin-orbit Interaction in Bilayer Graphene Encapsulated by WS₂ films. *Sci. Rep.* **8**, 3412 (2018).
 25. Ye, P., Yuan, R. Y., Zhao, X. & Guo, Y. Electric controlled spin and valley transport of massive electrons in graphene with spin-orbit coupling. *J. Appl. Phys.* **121**, 144302 (2017).
 26. Omar, S. & van Wees, B. J. Graphene-WS₂ heterostructures for tunable spin injection and spin transport. *Phys. Rev. B* **95**, 81404 (2017).
 27. Offidani, M., Milletar\`i, M., Raimondi, R. & Ferreira, A. Optimal Charge-to-Spin Conversion in Graphene on Transition-Metal Dichalcogenides. *Phys. Rev. Lett.* **119**, 196801 (2017).
 28. Huang, C., Chong, Y. D. & Cazalilla, M. A. Anomalous Nonlocal Resistance and Spin-Charge Conversion Mechanisms in Two-Dimensional Metals. *Phys. Rev. Lett.* **119**, 136804 (2017).
 29. Ando, Y. & Shiraishi, M. Spin to Charge Interconversion Phenomena in the Interface and Surface States. *J. Phys. Soc. Japan* **86**, 11001 (2016).
 30. Gurram, M., Omar, S. & van Wees, B. J. Electrical spin injection, transport, and detection in graphene-hexagonal boron nitride van der Waals heterostructures: progress and perspectives. *2D Mater.* **5**, 32004 (2018).
 31. Wang, Z. et al. Strong interface-induced spin-orbit interaction in graphene on WS₂. *Nat. Commun.* **6**, 8339 (2015).
 32. Benítez, L. A. et al. Strongly anisotropic spin relaxation in graphene-transition metal dichalcogenide heterostructures at room temperature. *Nat. Phys.* **14**, 303–308 (2018).
 33. Zhu, T. & Kawakami, R. K. Modeling the oblique spin precession in lateral spin valves for accurate determination of the spin lifetime anisotropy: Effect of finite contact resistance and channel length. *Phys. Rev. B* **97**, 144413 (2018).
 34. Tombros, N. et al. Anisotropic Spin Relaxation in Graphene. *Phys. Rev. Lett.* **101**, 46601 (2008).

-
35. Popinciuc, M. et al. Electronic spin transport in graphene field-effect transistors. *Phys. Rev. B* **80**, 214427 (2009).
 36. Guimarães, M. H. D. et al. Controlling Spin Relaxation in Hexagonal BN-Encapsulated Graphene with a Transverse Electric Field. *Phys. Rev. Lett.* **113**, 86602 (2014).
 37. Avsar, A. et al. Optospintronics in Graphene via Proximity Coupling. *ACS Nano* **11**, 11678–11686 (2017).
 38. Luo, Y. K. et al. Opto-Valleytronic Spin Injection in Monolayer MoS₂/Few-Layer Graphene Hybrid Spin Valves. *Nano Lett.* **17**, 3877–3883 (2017).
 39. Zomer, P. J., Guimarães, M. H. D., Brant, J. C., Tombros, N. & van Wees, B. J. Fast pick up technique for high quality heterostructures of bilayer graphene and hexagonal boron nitride. *Appl. Phys. Lett.* **105**, 13101 (2014).
 40. Yan, W. et al. A two-dimensional spin field-effect switch. *Nat. Commun.* **7**, 13372 (2016).
 41. Dankert, A. & Dash, S. P. Electrical gate control of spin current in van der Waals heterostructures at room temperature. *Nat. Commun.* **8**, 16093 (2017).
 42. Gurram, M., Omar, S. & Wees, B. J. van. Bias induced up to 100% spin-injection and detection polarizations in ferromagnet/bilayer-hBN/graphene/hBN heterostructures. *Nat. Commun.* **8**, 248 (2017).
 43. Ingla-Aynés, J., Guimarães, M. H. D., Meijerink, R. J., Zomer, P. J. & van Wees, B. J. 24 μm spin relaxation length in boron nitride encapsulated bilayer graphene. *Phys. Rev. B* **92**, 201410 (2015).
 44. Drögeler, M. et al. Spin Lifetimes Exceeding 12 ns in Graphene Nonlocal Spin Valve Devices. *Nano Lett.* **16**, 3533–3539 (2016).
 45. Gurram, M. et al. Spin transport in fully hexagonal boron nitride encapsulated graphene. *Phys. Rev. B* **93**, 115441 (2016).
 46. Maassen, T., Vera-Marun, I. J., Guimarães, M. H. D. & van Wees, B. J. Contact-induced spin relaxation in Hanle spin precession measurements. *Phys. Rev. B* **86**, 235408 (2012).

